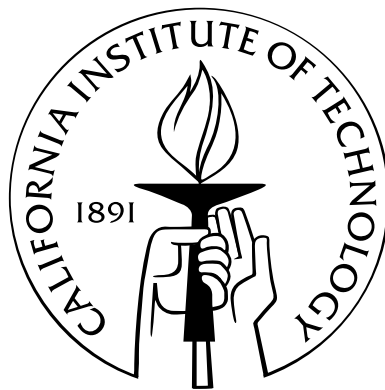


Semiconductor Optical Microcavities for Chip-Based Cavity QED

Thesis by
Kartik Srinivasan

In Partial Fulfillment of the Requirements
for the Degree of
Doctor of Philosophy



California Institute of Technology
Pasadena, California

2006
(Defended May 3, 2006)

© 2006

Kartik Srinivasan

All Rights Reserved

To my friends and family

Acknowledgements

The work described in this thesis would not have been possible without the contributions of a number of people. First and foremost, I would like to thank my advisor, Professor Oskar Painter, for the time and energy he has invested in my research and training as a scientist. Oskar's genuine enthusiasm and passion for physics are remarkable, as is his willingness to provide his students with tangible help with their research. In addition to his role as my advisor, I have also enjoyed his friendship over the years.

Since my undergraduate days at Caltech, I have benefited from the guidance of Professors Kerry Vahala and William Bridges. Professor Vahala gave me my first introduction to an optics research lab as a sophomore and my first industry job at XPonent Photonics after I graduated with my bachelor's degree, and my subsequent choices in research have been greatly influenced by these rewarding experiences and his mentorship. Professor Bridges served as my undergraduate advisor, and I appreciate the time and care he put into what is a largely unrecognized role.

There are a number of other researchers at Caltech and abroad that have played a part in shaping my time in graduate school. I appreciate the interactions I have had with Professors Amnon Yariv and Hideo Mabuchi, who are two scientists that I admire as researchers and teachers. During my first three years in graduate school, I greatly enjoyed a collaboration with the quantum cascade laser group at Bell Laboratories, and in particular, Dr. Raffaele Colombelli (now at Université Paris-Sud) and Professor Federico Capasso (now at Harvard). I would also like to thank Dr. Jianxin Chen of Bell Laboratories and Professors Andreas Stintz and Sanjay Krishna of the University of New Mexico, whose expertise in material growth has allowed us to undertake experiments that could not have been done at Caltech alone. Finally, I would like to acknowledge the Hertz Foundation for my graduate fellowship, and recognize the effort they put into identifying and funding promising students.

Oskar has assembled a talented and personable group of individuals with whom it has been a pleasure to work. I would particularly like to thank my officemate Paul Barclay. Paul and I have very

similar research interests, and I think we have been able to learn a lot from each other. Similarly, I have enjoyed interacting with Matt Borselli, who has been a great sounding board for ideas, and Tom Johnson, whom I have known since our time working together at XPonent. The four of us were Oskar's first graduate students, and the hard work and tedium of building a research lab was made easier because it was done with good friends. More recently, I have enjoyed collaborating with Chris Michael and Ben Lev (a student in Hideo's group), as well as interacting with Raviv Perahia, David Henry, Matt Eichenfield, Orion Crisafulli, and Jessie Rosenberg.

The biggest influence in my life has been my parents, and I want to thank my mom Kalpagam and my dad V.K. for their unconditional love and support, and the example they set for me. I also want to thank my older sister Jahnavi, who I have always looked up to. My oldest sister Meera and her husband Jon have lived 15 minutes away from me for the past ten years, and during that time, they have always kept their home open to me. I truly appreciate everything they have done for me, and the affection of my nieces Kiran and Jaya.

Finally, there a large number of friends from my undergraduate days that I should thank in detail, but will instead just thank as a group. I would, however, like to single out one person, Hanna Kim, for all her friendship and support over the years.

Abstract

Optical microcavities can be characterized by two key quantities: an effective mode volume V_{eff} , which describes the per photon electric field strength within the cavity, and a quality factor Q , which describes the photon lifetime within the cavity. Cavities with a small V_{eff} and a high Q offer the promise for applications in nonlinear optics, sensing, and cavity quantum electrodynamics (cavity QED). Chip-based devices are particularly appealing, as planar fabrication technology can be used to make optical structures on a semiconductor chip that confine light to wavelength-scale dimensions, thereby creating strong enough electric fields that even a single photon can have an appreciable interaction with matter. When combined with the potential for integration and scalability inherent to microphotonic structures created by planar fabrication techniques, these devices have enormous potential for future generations of experiments in cavity QED and quantum networks.

This thesis is largely focused on the development of ultras-small V_{eff} , high- Q semiconductor optical microcavities. In particular, we present work that addresses two major topics of relevance when trying to observe coherent quantum interactions within these semiconductor-based systems: (1) the demonstration of low optical losses in a wavelength-scale microcavity, and (2) the development of an efficient optical channel through which the sub-micron-scale optical field in the microcavity can be accessed. The two microcavities of specific interest are planar photonic crystal defect resonators and microdisk resonators.

The first part of this thesis details the development of photonic crystal defect microcavities. A momentum space analysis is used to design structures in graded square and hexagonal lattice photonic crystals that not only sustain high Q s and small V_{eff} s, but are also relatively robust to imperfections. These designs are then implemented in a number of experiments, starting with device fabrication in an InAsP/InGaAsP multi-quantum-well material to create low-threshold lasers with Q s of 1.3×10^4 , and followed by fabrication in a silicon-on-insulator system to create passive resonators with Q s as high as 4.0×10^4 . In the latter experiments, an optical fiber taper waveguide is used to couple light into and out of the cavities, and we demonstrate its utility as an optical

probe that provides spectral and spatial information about the cavity modes. For a cavity mode with $Q \sim 4 \times 10^4$, we demonstrate mode localization data consistent with $V_{\text{eff}} \sim 0.9(\lambda/n)^3$.

In the second part of this thesis, we describe experiments in a GaAs/AlGaAs material containing self-assembled InAs quantum dots. Small diameter microdisk cavities are fabricated with $Q \sim 3.6 \times 10^5$ and $V_{\text{eff}} \sim 6(\lambda/n)^3$, and with $Q \sim 1.2 \times 10^5$ and $V_{\text{eff}} \sim 2(\lambda/n)^3$. These devices are used to create room-temperature, continuous-wave, optically pumped lasers with thresholds as low as $1 \mu\text{W}$ of absorbed pump power. Optical fiber tapers are used to efficiently collect emitted light from the devices, and a laser differential efficiency as high as 16% is demonstrated. Furthermore, these microdisk cavities have the requisite combination of high Q and small V_{eff} to enable strong coupling to a single InAs quantum dot, in that the achievable coupling rate between the quantum dot and a single photon in the cavity is predicted to exceed the decay rates within the system. Quantum master equation simulations of the expected behavior of such fiber-coupled devices are presented, and progress towards such cavity QED experiments is described.

Contents

Acknowledgements	v
Abstract	vii
List of Figures	xix
List of Tables	xxi
Acronyms	xxii
Preface	1
List of Publications	34
I Development of Ultrasmall Volume, High-Q Photonic Crystal Microcavities	38
1 Semianalytic Methods for Studying Localized Modes Within Two-Dimensional Photonic Crystals	40
1.1 Symmetry-based analysis	40
1.1.1 Introduction	40
1.1.2 Hexagonal lattice photonic crystals	42
1.1.2.1 X-point	45
1.1.2.2 J-point	47
1.1.2.3 Conduction band donor modes	49
1.1.2.4 Valence band acceptor modes	54
1.1.3 Square lattice photonic crystals	57
1.1.3.1 X-point	58

1.1.3.2	M-point	61
1.1.3.3	Conduction band donor modes	62
1.1.3.4	Valence band acceptor modes	65
1.1.4	Comparison with FDTD simulations	66
1.2	Wannier-like approach for describing localized modes in photonic crystals	70
1.2.1	Introduction	70
1.2.2	Wannier theorem for photons in periodic dielectric structures	71
1.2.3	Envelope function calculation	79
1.2.3.1	Donor modes at the X -point	79
1.2.3.2	Acceptor modes at the J -point	87
2	Momentum Space Design of High-Q Photonic Crystal Microcavities	93
2.1	Introduction	93
2.2	Momentum space consideration of vertical radiation loss	94
2.3	Summary of the symmetry analysis of defect modes in hexagonal and square lattices	96
2.3.1	Hexagonal lattice	98
2.3.2	Square lattice	100
2.4	Initial FDTD simulation results	102
2.4.1	Hexagonal lattice	103
2.4.2	Square lattice	104
2.5	Momentum space design of the defect geometry in a square lattice	105
2.6	Tailoring of the defect geometry for the $\mathbf{H}_{A_2}^{a,a1}$ mode in the hexagonal lattice	112
2.7	Defect modes in a compressed hexagonal lattice	115
2.7.1	Preliminary analysis	115
2.7.2	FDTD results	119
2.8	Summary	121
3	High-Q Photonic Crystal Microcavities in InAsP/InGaAsP Multi-Quantum-Well Membranes	125
3.1	Introduction	125
3.2	Fabrication of PC cavities in InP-based multi-quantum-well membranes	127
3.2.1	Mask creation	128
3.2.2	InAsP/InGaAsP membrane etch and undercut	129

3.3	Photoluminescence measurements	133
3.4	Summary	136
4	Optical-Fiber-Based Measurement of an Ultrasmall Volume, High-Q Silicon Photonic Crystal Microcavity	138
4.1	Introduction	138
4.2	Fabrication	139
4.3	Measurement setup	140
4.4	Measurement results	143
4.4.1	Polarization	143
4.4.2	High- Q measurements	145
4.4.3	Spatial localization measurements	147
4.5	Applications to quantum optics	151
4.6	Fabrication-tolerant high- Q cavities	152
4.7	Fiber tapers as an optical probe for photonic crystal microcavities	157
4.8	Efficient optical fiber coupling to photonic crystal microcavities and microdisks	161
4.8.1	PC microcavities	161
4.8.2	Microdisk cavities	163
II	Fiber-Coupled Microdisk Cavities with Embedded Quantum Dots	165
5	Optical Loss and Lasing Characteristics of AlGaAs Microdisk Cavities with Embedded Quantum Dots	167
5.1	Introduction	167
5.2	Overview of microdisk cavity modes	168
5.2.1	Analytic approximation	168
5.2.2	Finite-element method simulations	171
5.2.3	Standing wave whispering gallery modes	172
5.3	Fabrication	174
5.4	Cavity Q measurements in the 1400 nm band	176
5.5	Initial measurements of lasing behavior	178

6	Photoluminescence Measurements of Quantum-Dot-Containing Microdisks Using Optical Fiber Tapers	181
6.1	Preliminary discussion and experimental methods	182
6.2	Measurement of cavity Q in the 1200 nm wavelength band	185
6.3	Improved collection efficiency with fiber tapers	187
6.4	Fiber-pumped microdisk lasers	193
6.5	Discussion and future applications	194
7	Cavity Q, Mode Volume, and Lasing Threshold in Small Diameter Microdisks with Embedded Quantum Dots	196
7.1	Simulations	196
7.2	Passive measurement of cavity Q	201
7.3	Measurements of lasing behavior	202
8	Prospects for Strong Coupling Between a Single Quantum Dot and Standing Wave Whispering Gallery Modes of a Semiconductor Microdisk Cavity	207
8.1	Introduction	207
8.2	Modal coupling of two whispering gallery modes due to surface scattering	210
8.3	Quantum master equation model	213
8.4	Solutions to the steady state quantum master equation in the weak driving regime	218
8.4.1	$\beta > g > (\kappa, \gamma_{\perp})$	219
8.4.2	$g > \beta > (\kappa, \gamma_{\perp})$	222
8.4.3	$\kappa > g > \beta > \gamma_{\perp}$	223
8.4.4	$\gamma_{\parallel} > g > \beta > \kappa$	224
8.4.5	$g > \kappa > \beta > \gamma_{\perp}$	224
8.4.5.1	Steady state analysis	224
8.4.5.2	Time-dependent analysis	225
8.4.6	$\beta = 0; g > \kappa > \gamma_{\perp}$	228
8.5	Potential for low power switching in the microdisk-QD system	229
9	Conclusions and Future Outlook	233

Appendixes

A	Quantum Cascade Photonic Crystal Surface-Emitting Injection Lasers	237
A.1	Introduction	237
A.2	Basic design and fabrication	238
A.3	Electroluminescence and lasing measurements	240
B	Finite-Difference Time-Domain Simulations	245
C	Fabrication Notes	249
C.1	Process flow and general considerations	249
C.2	Si-based devices	252
C.3	AlGaAs-based devices	254
C.4	ICP-RIE etching of quantum cascade heterostructures	257
D	Cavity Q and Related Quantities	260
E	Resonator-Waveguide Coupled Mode Theory	263
E.1	Traveling wave mode resonator	263
E.2	Standing wave mode resonator	268
F	Laser Rate Equations	270
G	The Jaynes-Cummings Model	274
G.1	The Jaynes-Cummings Hamiltonian and eigenvalue spectrum	274
G.2	The damped, driven Jaynes-Cummings model	278
G.2.1	Driving field	278
G.2.2	Dissipation terms and the quantum master equation approach	280
H	The Purcell Factor F_p and Atom-Photon Coupling Rate g	284
H.1	The Purcell factor	284
H.2	Atom-photon coupling rate	287
	Bibliography	289

List of Figures

1	Schematic of quantum-dot-photon coupling in a photonic crystal cavity.	3
1.1	Illustration of a two-dimensional photonic crystal cavity in a slab waveguide structure.	41
1.2	Bandstructure and real and reciprocal space representations of a hexagonal lattice photonic crystal	43
1.3	X-point valence and conduction band modes in a hexagonal lattice photonic crystal .	47
1.4	J-point valence and conduction band modes in a hexagonal lattice photonic crystal .	49
1.5	Example defect cavity geometries in the hexagonal lattice.	50
1.6	Conduction band donor modes in a hexagonal lattice photonic crystal	53
1.7	Valence band acceptor modes in a hexagonal lattice photonic crystal	55
1.8	X-point valence band acceptor modes in a hexagonal lattice photonic crystal	57
1.9	Bandstructure and real and reciprocal space representations of a square lattice photonic crystal	58
1.10	X-point valence and conduction band modes in a square lattice photonic crystal . . .	60
1.11	M-point valence and conduction band modes in a square lattice photonic crystal . . .	62
1.12	Conduction band donor modes in a square lattice photonic crystal	64
1.13	Valence band acceptor modes in a square lattice photonic crystal	66
1.14	FDTD-generated spectrum of a single defect PC cavity	67
1.15	Dipole-like modes in a photonic crystal cavity.	69
1.16	Graded hexagonal lattice donor- and acceptor-type cavities.	85
1.17	Comparison of donor modes in a graded hexagonal lattice cavity as generated by the Wannier/symmetry analysis and FDTD simulations.	86
1.18	Comparison of acceptor modes in a graded hexagonal lattice cavity as generated by the Wannier/symmetry analysis and FDTD simulations.	92
2.1	2D hexagonal PC slab waveguide structure and cladding light cone.	95

2.2	Real and reciprocal space representations of 2D hexagonal and square lattice photonic crystals.	96
2.3	Spatial Fourier transform of E_x of the x -dipole donor mode in a hexagonal lattice. . .	97
2.4	Fundamental TE-like (even) guided mode bandstructure for hexagonal and square lattices.	98
2.5	Illustration showing the mode coupling for the $\mathbf{H}_{A2}^{e,d1}$ mode in \mathbf{k} -space through the $\widetilde{\Delta\eta}$ perturbation.	107
2.6	$\widetilde{\Delta\eta}(\mathbf{k}_\perp)$ for dielectric structure of table 2.7.	108
2.7	Properties of the graded square lattice.	109
2.8	(a) $\widetilde{\Delta\eta}(\mathbf{k}_\perp)$ for single enlarged hole design in hexagonal lattice ($r/a = 0.30$, $r'/a = 0.45$). (b) $\widetilde{\Delta\eta}(\mathbf{k}_\perp)$ for graded hexagonal lattice design shown in table 2.9.	114
2.9	(a) Real and reciprocal space versions of a compressed 2D hexagonal lattice. (b) Fundamental TE-like guided mode bandstructures for a compressed hexagonal lattice.	116
2.10	Modal characteristics of a simple defect mode in a compressed hexagonal lattice ($d/a = 0.75$).	120
3.1	FDTD-calculated properties of the graded square lattice PC cavity design.	126
3.2	Angled view SEM image of the SiO_2 etch mask	128
3.3	Cross-sectional SEM images of InP ICP-RIE etches.	130
3.4	Wet etch characteristics of the InP sacrificial layer.	131
3.5	Comparison of CAIBE and ICP-RIE etches of InP-based PC lasers.	132
3.6	Top view SEM image of a fabricated PC cavity.	133
3.7	Schematic of the photoluminescence measurement setup.	134
3.8	L-L curves and subthreshold emission spectra from PC microcavity lasers under different pump conditions.	135
3.9	Localization and polarization measurements of the PC microcavity laser mode. . . .	136
4.1	SEM images of Si PC microcavities.	140
4.2	Zoomed-in SEM images of a Si PC microcavity.	141
4.3	Measurement setup for fiber taper probing of PC microcavities.	142
4.4	Polarization measurements of PC microcavity modes using the fiber taper.	144
4.5	Summary of the graded square lattice PC cavity design.	145
4.6	Q measurements in a PC microcavity using the fiber taper.	146

4.7	PC microcavity mode localization measurements using the fiber taper.	148
4.8	Mode localization measurements of a higher order mode in the graded square lattice PC microcavity.	150
4.9	Resolution of the fiber taper.	151
4.10	Grade in the normalized hole radius for different square lattice PC cavities.	155
4.11	Q measurements for two of the PC cavity devices of fig. 4.10 and table 4.1.	157
4.12	Fiber-coupled PC microcavity using an intermediate PC waveguide.	162
4.13	SEM image of a Si microdisk cavity.	164
5.1	Schematic and photoluminescence of a 1DWELL epitaxy.	175
5.2	SEM images of DWELL-containing microdisk cavities	176
5.3	Q measurements of 4.5 μm diameter AlGaAs microdisk cavities in the 1400 nm band	177
5.4	Photoluminescence measurements of 4.5 μm diameter microdisk cavities with em- bedded quantum dots.	179
6.1	Experimental setup for studying the QD-microdisk devices with fiber tapers.	184
6.2	Passive measurements of DWELL-containing AlGaAs microdisks in the 1200 nm band.	187
6.3	Comparison of free-space and fiber taper collection.	188
6.4	(a) L-L curves for free-space pumping and fiber taper collection at different taper positions. (b) Scatter plot of the differential efficiency for fiber taper (filled circles) and free-space collection (open circles) for a number of different microdisk lasers. . .	190
6.5	Light-in-light-out characteristic for lasing and non-lasing modes.	191
6.6	Light-in-light-out curve and subthreshold spectrum for fiber-pumped microdisk laser.	194
7.1	SEM image and finite element calculation of the electric field intensity for a $D \sim 2\mu\text{m}$ diameter microdisk.	197
7.2	Finite-element simulation results for Q_{rad} and V_{eff} (and the implied g and κ) as a function of disk diameter.	198
7.3	Calculated $g/\max(\gamma_{\perp}, \kappa)$ as a function of microdisk diameter.	199
7.4	Comparison of finite-element-calculated electric field intensity in disks with vertical and slanted sidewalls.	200
7.5	PL spectrum from the 1.3 μm 1DWELL epitaxy and Q measurement for a 2 μm diameter microdisk fabricated from this material.	202

7.6	Light-in-light-out curve for a 2 μm diameter quantum-dot-embedded microdisk device operated with free-space collection.	203
7.7	Comparison of L-L curves from a 2 μm diameter quantum-dot-embedded microdisk using free-space and fiber-based collection.	204
7.8	Rate equation model fit to experimental data from a fiber taper coupled microdisk laser.	205
8.1	Illustrations of the various experimental configurations utilized in studying coupling between a semiconductor microdisk and a single QD.	209
8.2	Calculated doublet mode spectra for different parameter regimes.	212
8.3	Finite-element method calculated V_{eff} of traveling wave modes of a microdisk cavity.	219
8.4	Normalized transmitted and reflected signal for a QD coupled to a microdisk cavity, calculated through numerical solution of the steady state quantum master equation under weak driving, for $g/2\pi=6$ GHz, $\beta/2\pi=9.6$ GHz, $\kappa/2\pi=1.2$ GHz, and $\tau_{\text{sp}}=1$ ns.	220
8.5	Calculated normalized transmitted and reflected signal for a QD coupled to a microdisk cavity, using identical parameters as those used in fig. 8.4, but with $\beta/2\pi=-9.6$ GHz.	221
8.6	Calculated normalized transmitted and reflected signal for a QD coupled to a microdisk cavity, using identical parameters as those used in fig. 8.4, but with $\beta/2\pi=i*9.6$ GHz ($i = \sqrt{-1}$).	222
8.7	Calculated normalized transmitted and reflected signal for a QD coupled to a microdisk cavity, for the regimes (a) $g > \beta > (\kappa, \gamma_{\perp})$, (b) $\kappa > g > \beta > \gamma_{\perp}$, (c) $\gamma_{\parallel} > g > \beta > \kappa$, and (d) $g > \kappa > \beta > \gamma_{\perp}$	223
8.8	Normalized transmitted signal for a QD coupled to a microdisk cavity, calculated as a function of time through numerical integration of the quantum master equation under weak driving.	225
8.9	Number of intracavity photons in the microdisk clockwise and counterclockwise propagating WGMs, calculated by numerical integration of the quantum master equation.	226
8.10	Calculated normalized transmitted and reflected signal for a QD coupled to a microdisk cavity, for $\beta=0$	228

8.11	Steady state solutions to the semiclassical Maxwell-Bloch equations and quantum master equation, showing normalized intracavity field amplitude $ X_{ss} $ as a function of normalized drive field Y	230
8.12	Steady state solutions to the semiclassical Maxwell-Bloch equations and quantum master equation, showing cavity reflection as a function of average number of intracavity drive photons and input drive power, for varying cavity decay rates.	231
8.13	Steady state solutions to the semiclassical Maxwell-Bloch equations and quantum master equation, showing normalized intracavity field amplitude $ X_{ss} $ as a function of normalized drive field $ Y $, for a system with large non-radiative dephasing (linewidth ~ 5 meV).	232
8.14	Steady state solutions to the quantum master equation, showing cavity reflection as a function of average number of intracavity drive photons and input drive power, for a system with large non-radiative dephasing (linewidth ~ 5 meV)	232
A.1	Schematic, SEM image, in-plane bandstructure, and subthreshold and lasing spectra for a QC-PCSEL.	239
A.2	Surface plasmon mode and cross sectional SEM image of a QC PCSEL device.	240
A.3	Multi-wavelength emission in a QC-PCSEL array.	241
A.4	Polarized emission patterns and FDTD-simulations for a QC-PCSEL device.	242
A.5	Measurements and FDTD simulations of the QC-PCSEL far field emission pattern	243
B.1	Setup for FDTD simulations.	246
B.2	FDTD spectra and mode field patterns for TM-polarized donor type defect modes in a square lattice photonic crystal.	247
C.1	Process flow for fabrication of microphotonic devices such as photonic crystals.	250
C.2	SEM images of the Si ICP-RIE etch with varying gas flow and RF power.	253
C.3	Angled and top view SEM images of the Si etch used in fabrication of high- Q PC cavities.	253
C.4	Top view and cross sectional SEM images of AlGaAs PC cavities fabricated using an SiO ₂ etch mask.	254
C.5	SEM images of AlGaAs photonic crystals using direct pattern transfer from an electron beam mask.	255

C.6	SEM images of photonic crystal patterns in a SiN_x mask and subsequent transfer into AlGaAs.	256
C.7	SEM images of photonic crystal and microdisk patterns when the SiN_x etch does not turn out properly, most likely because of too low a flow of C_4F_8	257
C.8	SEM images of a typical QC-PCSEL device after the semiconductor etch, but before the deposition of electrical contacts.	259
E.1	Schematic for single mode coupling between a resonator and waveguide.	263
G.1	Schematic for atom-field coupling and block diagonal form for the Hamiltonian in the Jaynes-Cummings model.	276
G.2	Energy level spectrum for the Jaynes-Cummings model ($\omega_f = \omega_a$).	277

List of Tables

1	Optical microcavities in 2002	4
2	Optical microcavities in 2006	32
1.1	Point group character tables for the hexagonal lattice.	44
1.2	Point group character tables for the square lattice.	59
1.3	FDTD calculations of modes in a single defect hexagonal lattice PC cavity	68
1.4	Hexagonal PC parameters for the donor- and acceptor-type defect cavities.	85
1.5	Donor mode (X -point) ground state Wannier envelope parameters.	85
1.6	FDTD calculated mode envelope parameters.	87
1.7	Acceptor mode (J -point) ground state Wannier envelope parameters	91
2.1	Symmetry classification and dominant Fourier components for the \mathbf{H} -field of conduction band donor modes in a hexagonal lattice.	99
2.2	Symmetry classification and dominant Fourier components for the \mathbf{H} -field of valence band acceptor modes in a hexagonal lattice.	100
2.3	Symmetry classification and dominant Fourier components for the \mathbf{H} -field of conduction band donor modes in a square lattice.	101
2.4	Symmetry classification and dominant Fourier components for the \mathbf{H} -field of valence band acceptor modes in a square lattice.	101
2.5	Candidate donor and acceptor modes in a square lattice.	102
2.6	Characteristics of the $\mathbf{H}_{A_2}^{a,a1}$ resonant mode in a hexagonal lattice	104
2.7	Characteristics of the $\mathbf{H}_{A_2}^{e,d1}$ resonant mode in a square lattice	105
2.8	Field characteristics of the graded square lattice shown in fig. 2.7(a).	110
2.9	FDTD simulation results for graded hexagonal lattice geometries	113
2.10	Key geometrical quantities associated with the standard and compressed hexagonal lattices.	117

2.11	FDTD simulation results for graded compressed hexagonal lattice geometries.	121
3.1	Epitaxy for 1.3 μm PC microcavity lasers	127
4.1	Theoretical and experimental Q factors for PC cavities with r/a profiles shown in fig. 4.10.	156
5.1	Epitaxy for 1-DWELL microcavity lasers.	175
7.1	Finite-element calculated $\text{TE}_{p=1,m}$ modes of a $D = 2 \mu\text{m}$ microdisk.	201

Acronyms

cQED, or **cavity QED** Cavity quantum electrodynamics

DBR Distributed Bragg reflection

DWELL Epitaxy consisting of a layer of quantum dots embedded in a quantum well (dot-in-a-well)

EL Electroluminescence

FEMLAB Commercial software, written by the Comsol Group, for solving partial differential equations by the finite element method

FDTD Finite-difference time-domain

FSR Free spectral range

ICP-RIE Inductively coupled plasma reactive ion etch

MBE Molecular beam epitaxy

MQW Multi-quantum-well

NA Numerical aperture

OSA Optical spectrum analyzer

PC Photonic crystal

PCWG Photonic crystal waveguide

PECVD Plasma enhanced chemical vapor deposition

PL Photoluminescence

Q Quality factor

QC Quantum cascade

QC-PCSEL Quantum cascade photonic crystal surface-emitting laser

QD Quantum dot

SEM Scanning electron microscope

SOI Silicon-on-insulator

TE Transverse electric polarization, defined in this thesis to have electric field components predominantly in-plane and a magnetic field primarily out-of-plane

TM Transverse magnetic polarization, defined in this thesis to have magnetic field components predominantly in-plane and an electric field primarily out-of-plane

V_{eff} Effective mode volume

WGM Whispering gallery mode

WG Waveguide

